PAPER

Check for updates

Crystal growth and magnetic properties of hexagonal Ba$_4$CuNb$_3$O$_{12}$ single crystals†

Yuhu Huang,[a] Wen Xie,[ab] Fei Zheng,[c] Chao Zhang*[d] and Han-Shu Xu [iD] *[ab]

We report a systematic investigation of the growth of high-quality hexagonal perovskite Ba$_4$CuNb$_3$O$_{12}$ single crystals using the flux method. The optimal growth involved using the tetragonal phase BaCu$_{0.33}$Nb$_{0.67}$O$_3$ as the precursor, with 20 g CuO as the flux, a cooling rate of 1 °C h^{-1} between 1350 °C and 1100 °C, and a cooling rate of 2 °C h^{-1} from 1100 °C to 930 °C. The magnetic properties along the *ab*-plane and the perpendicular direction are thoroughly studied. Fitting the inverse magnetic susceptibility data from 2 K to 300 K with the modified Curie–Weiss (CW) law yields a Weiss temperature (θ_{CW}) of −1.14 K, indicating the presence of antiferromagnetic correlations in the ground state between Cu^{2+} ions *via* superexchange interactions. Furthermore, the specific heat data of Ba$_4$CuNb$_3$O$_{12}$ align well with the Debye–Einstein phonon model, allowing us to estimate the Debye temperature of 199 K and the average phonon velocity of 2014.98 m s^{-1}.

1. Introduction

Hexagonal perovskite oxides have garnered increasing attention due to their rich physicochemical properties and potential applications.[1–3] Their crystal structures are of the hexagonal perovskite type, characterized by the stacking of BO$_6$ octahedra along the *c*-axis in different arrangements, with the B-site typically occupied by a transition metal. For instance, Xu *et al.* first reported the synthesis of two-dimensional triangular frustrated Ba$_3$CoNb$_2$O$_9$ single crystals[4] and quasi-one-dimensional Sr$_6$Co$_5$O$_{15}$ single crystals doped with different amounts of Fe elements.[5] Li *et al.* synthesized a hexagonal perovskite oxide (2H, 6H, and 10H)-BaCo$_{0.9}$Ru$_{0.1}$O$_{3−\delta}$ with different [BaO$_3$] layers in a unit cell and systematically explored its electrocatalytic oxygen evolution performance.[6] Although 8H-hexagonal perovskite oxides are relatively common, as seen in systems like Ba$_8$Ti$_3$Ta$_4$O$_{24}$,[7] Ba$_4$LiM$_3$O$_{12}$ (M = Nb and Ta),[8,9] Ba$_8$Ti$_3$Nb$_4$O$_{24}$,[10,11] Ba$_4$Na$_3$RuO$_{12}$,[12] and Ba$_8$MnNb$_6$O$_{24}$,[13] 8H-hexagonal perovskites containing copper atoms are very rare. It is also worth noting that, in addition to the detailed study of the magnetism of

Ba$_8$MnNb$_6$O$_{24}$, which confirmed a 120° ordering ground state below the antiferromagnetic transition temperature T_N = 1.45 K,[14] research on the other 8H-hexagonal perovskite materials often focuses primarily on their crystal structure, with limited studies on their magnetic properties.[12]

The 8H-hexagonal perovskite structure requires a high coordination number between ions, with the size and charge of the A-site and B-site ions needing to meet specific conditions. Copper ions are prone to redox reactions, especially the conversion between Cu^{2+} (S = 1/2) and Cu$^+$ (non-magnetic S = 0). This redox behavior can lead to structural instability or phase transition, further limiting the stability of copper-containing compounds in the 8H-hexagonal perovskite oxides. As a typical example of 8H-hexagonal perovskite oxides, Ba$_4$CuNb$_3$O$_{12}$ crystallizes in the $P6_3/mmc$ space group, and the Nb1O$_6$ octahedron along the *c*-axis shares corners with the face-sharing (Nb2/Cu)O$_6$ octahedron, as illustrated in Fig. 1(a). Furthermore, the structural projection onto the *ab*-plane reveals that Nb1 atoms form a honeycomb structure, while Nb2/Cu atoms arrange in a triangular lattice, as shown in Fig. 1(b). Since Kumada *et al.* first synthesized Ba$_4$CuNb$_3$O$_{12}$ polycrystalline powders,[15] there have been no reports on their physical properties, nor have any single crystal studies been published to date. If Cu forms a perfect triangular lattice system in this system, the presence of geometric frustration could lead to the system exhibiting a spin liquid or quantum spin liquid ground state.[16] However, the random occupation of Nb2 and Cu atoms in Ba$_4$CuNb$_3$O$_{12}$ disrupts the perfect triangular lattice structure, similar to the site mixing of Mg^{2+} and Ga^{3+} in YbMgGaO$_4$,[17,18] yet the magnetic ground state of Ba$_4$CuNb$_3$O$_{12}$ remains an interesting subject for further exploration.

[a] *Hefei National Research Center for Physical Sciences at the Microscale, University of Science and Technology of China, Hefei 230026, China. E-mail: xhs@ustc.edu.cn*
[b] *Department of Applied Physics, Anhui Medical University, Hefei 230032, China*
[c] *School of Earth and Space Sciences, University of Science and Technology of China, Hefei 230026, China*
[d] *Instrumentation and Service Center for Physical Science, Westlake University, Hangzhou 310024, China. E-mail: zhangchao68@westlake.edu.cn*
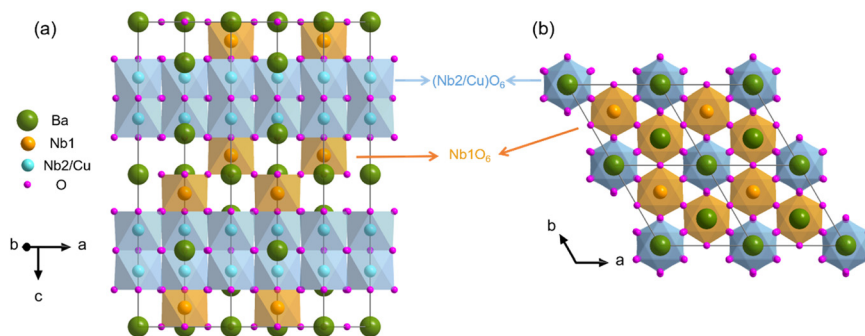† Electronic supplementary information (ESI) available. See DOI: https://doi.org/10.1039/d5ce00085h

Fig. 1 (a) Crystal structure of $Ba_4CuNb_3O_{12}$. (b) Projection of the crystal structure onto the *ab*-plane.

In this study, we conducted a comprehensive investigation of the growth of $Ba_4CuNb_3O_{12}$ single crystals using the flux method, thereby identifying the optimal synthesis route. We also examined the magnetism of the $Ba_4CuNb_3O_{12}$ single crystal both along and perpendicular to the *ab*-plane. Our results confirm that its ground state is antiferromagnetic. The specific heat behavior of $Ba_4CuNb_3O_{12}$ is in good agreement with that of the Debye–Einstein phonon model, and furthermore, it can be concluded that the average phonon velocity is 2014.98 m s^{-1}.

2. Characterization section

The single crystal structure and elemental composition were characterized at 298 K using X-ray diffraction (XRD, Rigaku SmartLab SE diffractometer), energy-dispersive spectroscopy (EDS, JEOL JSM-6700F), X-ray fluorescence (XRF, XRF-1800), and X-ray photoelectron spectroscopy (XPS, ESCALAB250Xi). Magnetization measurements were performed with a magnetic property measurement system (MPMS3, Quantum Design), while the specific heat was measured using the relaxation method on a physical property measurement system (PPMS, Quantum Design). In particular, in the measurement process of the direct current magnetic susceptibility (χ) of field-cooling (FC) the temperature rise test is adopted, namely the field cooled warming (FCW) process. In the single crystal XRD characterization, the tested single crystal is millimeter-sized, and the sample used for magnetic and specific heat measurements is taken from the single crystal shown in the upper right corner of Fig. 5(a), with a mass of 6.52 mg.

3. Synthesis steps of $Ba_4CuNb_3O_{12}$ single crystals

3.1 Synthesis of polycrystalline precursors

We first fully ground $BaCO_3$ (SCR, 99%), CuO (SCR, 99%), and Nb_2O_5 (SCR, 99%) in a molar ratio of 3 : 1 : 1, and then transferred the mixture to an Al_2O_3 crucible and calcined it at 1200 °C for 48 hours. From the XRD patterns in Fig. 2, we can observe that the main phase of the product is $BaCu_{0.33}Nb_{0.67}O_3$ with the *P4/mmm* space group, along with some impurity phase $Ba_5Nb_4O_{15.33}$, unreacted Nb_2O_5 and BaO

formed after the high-temperature decomposition of $BaCO_3$. Our next step is to use these polycrystalline powders to prepare single crystals *via* the flux method. In addition, from the perspective of single crystal growth, a small amount of the impure phase in the polycrystalline powder does not significantly affect the final crystal quality, as the type and proportion of the flux, along with the reaction temperature, are the key factors.[5]

3.2 Exploration of the best method for single crystal synthesis

3.2.1 Method I. The $BaCu_{0.33}Nb_{0.67}O_3$ polycrystalline powder was weighted to 5 g and mixed with 10 g of CuO as a flux. The mixture was thoroughly ground for about half an hour and then transferred into a 50 ml Al_2O_3 crucible. The Al_2O_3 crucible, sealed with a high-temperature ceramic sealant, was placed into a muffle furnace. It was heated to 1350 °C and held for 1 hour, then cooled down to 1100 °C at a rate of 1 °C h^{-1}, further cooled to 930 °C at 2 °C h^{-1}, and finally, the muffle furnace power was turned off. At room temperature, the sealed Al_2O_3 crucible was broken open, revealing that the entire crucible had turned brown, with no
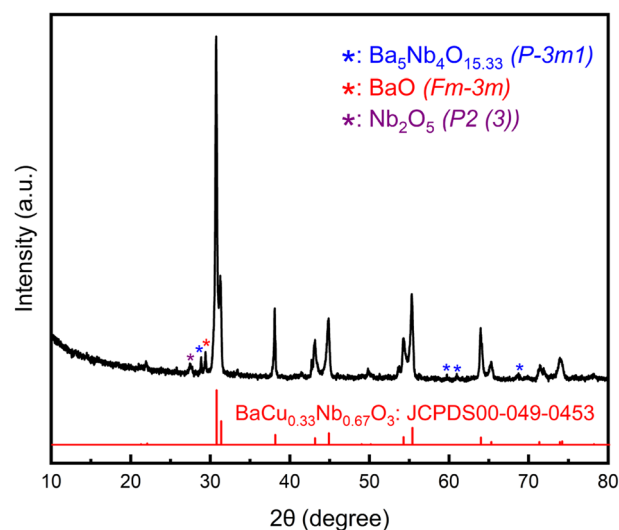

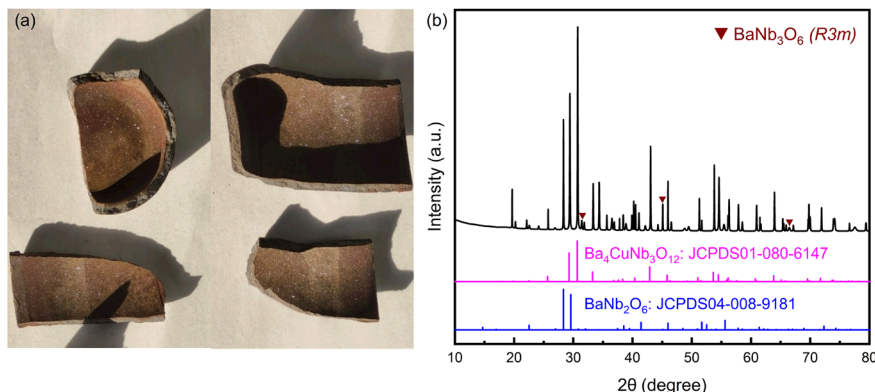**Fig. 2** XRD patterns of the obtained polycrystalline samples.

Fig. 3 (a) The crucible and the product obtained using method I. (b) XRD results of the product after thorough grinding.

single crystals formed, as shown in Fig. 3(a). To further determine the crystal structure of the final product, the material was scraped from the crucible wall using a blade and then XRD testing was performed.

The XRD results show that the synthesized product contains our target compound, the hexagonal perovskite $Ba_4CuNb_3O_{12}$, along with an additional phase of $BaNb_2O_6$ with the *Pmma* space group. Moreover, the product also contains a small amount of $BaNb_3O_6$ with the *R3m* space group. This suggests that during the process of single crystal growth, the crystal system of the obtained product may differ from that of the raw material. At 1350 °C, which is above the melting point of CuO, the mixture must be in a molten state, and as the temperature gradually decreases, the different elements can recombine to form new phases. Although no single crystal was obtained *via* method I, the target hexagonal crystal system $Ba_4CuNb_3O_{12}$ is synthesized, and additionally, the remaining product adhered to the crucible is very small, so in the improved method, the amount of the CuO flux should be increased.

3.2.2 Method II. To obtain high-quality single crystals of $Ba_4CuNb_3O_{12}$, we made slight adjustments to synthesis method I, increasing the CuO flux to 15 g while keeping the other reaction conditions unchanged. It is noteworthy that we successfully

synthesized sheet-like single crystals of $Ba_4CuNb_3O_{12}$ using method II, with approximate dimensions of (1.5–2.0) mm × (0.6–1.0) mm × (0.3–0.4) mm (inset of Fig. 4(b)), which has never been reported before. The single crystal X-ray diffraction results show that its surface corresponds to the (00*l*) crystal system (Fig. 4(b)), meaning that the surface of the sheet-like single crystal is the *ab*-plane.

Furthermore, to assess the quality of the crystals, we ground the obtained single crystals into powder and performed XRD characterization, as shown in Fig. 4(a). The results show that a small amount of $BaNb_3O_6$ is still in the $Ba_4CuNb_3O_{12}$ single crystals, due to the gradual growth of the crystal nucleus during the crystallization process of $Ba_4CuNb_3O_{12}$, which partially encapsulated and generated the formed $BaNb_3O_6$. Additionally, compared to method I, the product synthesized using method II does not contain the $BaNb_2O_6$ phase. Interestingly, by simply adjusting the content of the CuO flux, we can not only obtain single crystals but also further reduce the amount of the impurity phase.

3.2.3 Method III. We chose to continue to increase the mass of the CuO flux to 20 g, and the rest of the growth conditions were the same as in method I, which is referred to here as method III. Interestingly, the *ab*-plane of the single crystal $Ba_4CuNb_3O_{12}$ we obtained is hexagonal, which is

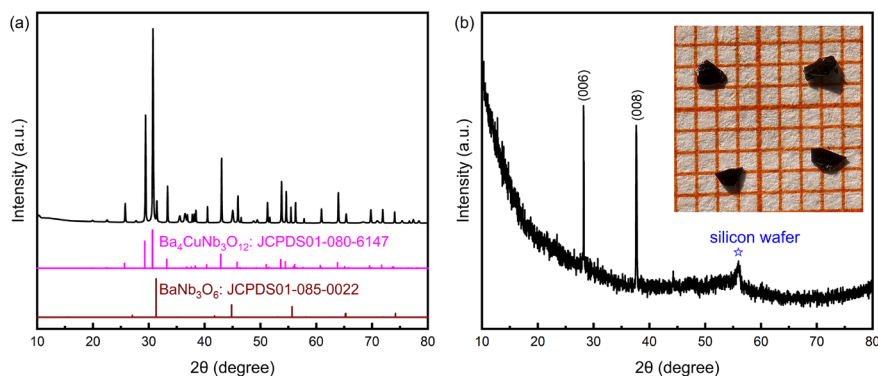**Fig. 4** (a) Powder XRD pattern of the $Ba_4CuNb_3O_{12}$ sample synthesized by method II. (b) The (00*l*) diffraction pattern of the $Ba_4CuNb_3O_{12}$ single crystal. Inset: Photograph of single crystals, with each small grid representing 1 mm. The blue star represents the sample holder silicon wafer signal.
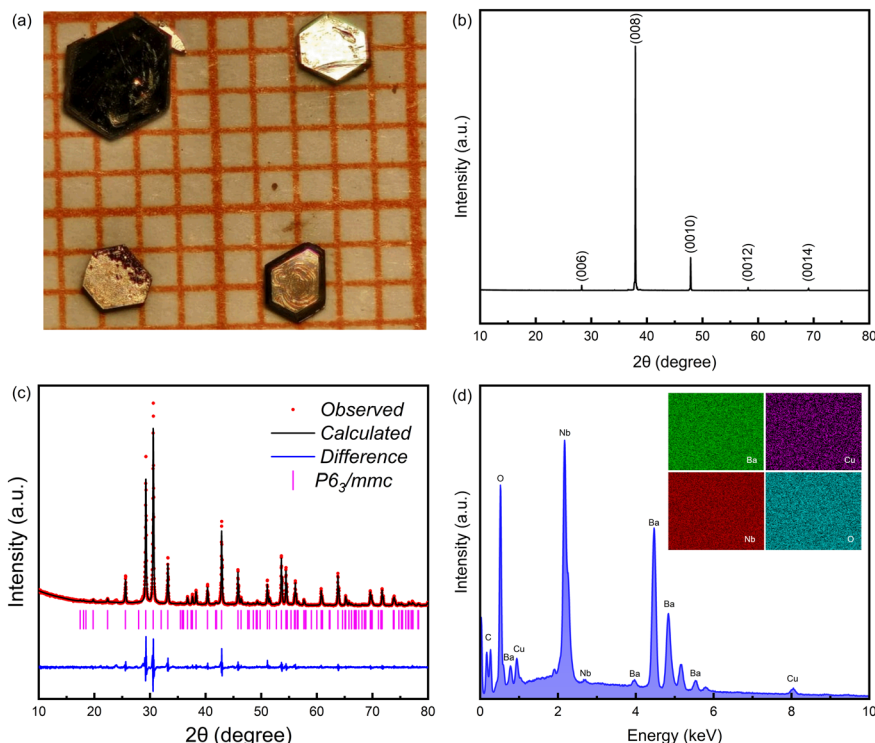
Fig. 5 (a) Photograph of the $Ba_4CuNb_3O_{12}$ single crystal, with each small grid representing 1 mm. (b) The (00l) diffraction pattern of the $Ba_4CuNb_3O_{12}$ single crystal. (c) Powder XRD pattern of $Ba_4CuNb_3O_{12}$. (d) EDS spectrum and elemental mapping (inset).

consistent with the sixfold symmetry of the crystal structure, and the size of the largest single crystal is about 3.0 mm × 3.0 mm × 0.5 mm (Fig. 5(a)). Furthermore, the XRD results of the $Ba_4CuNb_3O_{12}$ single crystal show only sharp (00l) peaks in the range of 10–80°, confirming its very high crystallinity (Fig. 5(b)). The high-quality single crystals of $Ba_4CuNb_3O_{12}$ were fully ground and tested by XRD, and the results confirmed that the obtained phase is pure. As shown in Fig. 5(c), the XRD refinement results show that the unit cell parameters of $Ba_4CuNb_3O_{12}$, belonging to the $P6_3/mmc$ space group, are $a = b = 5.7830(4)$ Å and $c = 18.9289(6)$ Å, and the detailed refinement parameters are presented in Table 1.

The EDS analysis clearly shows the presence of the elements Ba, Cu, Nb, and O, while the C element originates from the conductive carbon glue (Fig. 5(d)). Additionally, the EDS mapping reveals that Ba, Cu, Nb, and O are uniformly distributed across the tested area (inset of Fig. 5(d)). The EDS results indicate that the ratio of Cu and Nb elements is close to 1 : 3, but the Ba content is significantly higher, likely due to the presence of residual $BaCO_3$ or BaO attached on the surface (Fig. S1†). Furthermore, we ground the $Ba_4CuNb_3O_{12}$ single crystals into polycrystalline powder with a mass of about 25 mg and performed XRF testing (Fig. S1†). The results showed that the ratio of Ba, Cu and Nb is 4 : 1.85 : 2.38, which is similar to the results given by Kumada et al.[15] However, in order to maintain consistency with the previous work,[15] we still used the expression form $Ba_4CuNb_3O_{12}$ throughout the full text. In the chemical formula Ba_4CuNb_3-O_{12}, Ba ions have a +2 valence state, and Nb ions are +5. To

ensure charge balance in the formula, Cu ions must be +1. However, under the high-temperature conditions of single crystal growth, some Cu^+ will be converted into Cu^{2+}. As shown in Fig. S2,† the XPS results show that the ratio of Cu^+ to Cu^{2+} is approximately 1.12 : 1, and it should be noted that Cu^+ is non-magnetic ($S = 0$), while Cu^{2+} is magnetic ($S = 1/2$).

3.2.4 Method IV and method V. Among the three synthesis methods mentioned above, we successfully achieved the first synthesis of high-quality $Ba_4CuNb_3O_{12}$ single crystals by simply adjusting the CuO flux content. However, to further

Table 1 Crystal data and structure refinement for $Ba_4CuNb_3O_{12}$

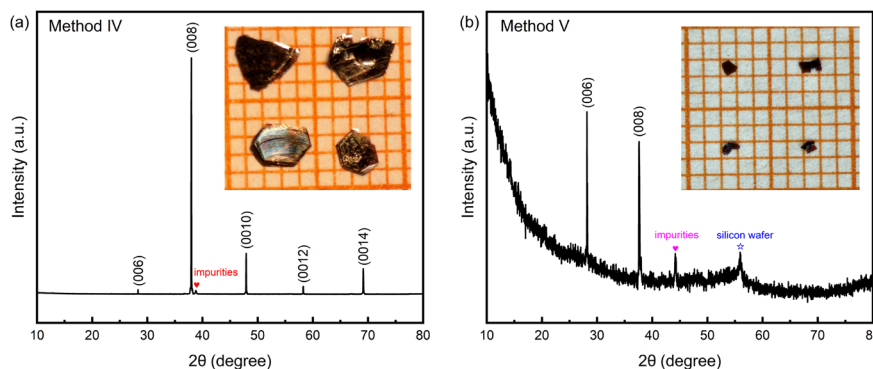| Parameter			Value		
Compound			$Ba_4CuNb_3O_{12}$		
Space group			$P6_3/mmc$		
a/b/Å			5.7830(4)		
c/Å			18.9289(6)		
Cell volume/Å³			548.23(5)		
R_{wp}/%			9.22		
R_p/%			7.04		
χ^2			5.01		
Atom	Wyck.	Site	x/a	y/b	z/c
Ba1	2a	-3m.	0	0	0
Ba2	2d	-6m2	1/3	2/3	3/4
Ba3	4f	3m.	1/3	2/3	0.13488
Nb4	4f	3m.	1/3	2/3	9/16
Nb5	4e	3m.	0	0	0.1829
Cu6	4e	3m.	0	0	0.1829
O7	6g	.2/m.	1/2	0	0
O8	6h	mm2	0.161	0.322	1/4
O9	12k	.m.	0.82642	0.65284	0.1187

Fig. 6 The (00*l*) diffraction patterns of the $Ba_4CuNb_3O_{12}$ single crystal synthesized by (a) method IV and (b) method V. Inset: Photograph of the $Ba_4CuNb_3O_{12}$ single crystal, with each small grid representing 1 mm.

optimize the synthesis method, we made additional improvements based on method III. In method IV, we kept the CuO flux amount constant at 20 g and adjusted the cooling rate to 1.5 °C h^{-1} within the temperature range of 1350 °C to 1100 °C. In method V, we further adjusted the cooling rate in this temperature zone to 3 °C h^{-1}. The $Ba_4CuNb_3O_{12}$ single crystals synthesized by method IV and method V are shown in Fig. 6(a) and (b), respectively. Compared to method III, a slight increase in the cooling rate to 1.5 °C h^{-1} has little effect on the size and crystal quality of the $Ba_4CuNb_3O_{12}$ single crystal, as shown in Fig. 6(a). However, when the cooling rate is significantly increased to 3.0 °C h^{-1}, the size of the synthesized single crystal is significantly reduced, and its crystallinity deteriorates. For Pb_2CoWO_6 single crystal growth, reducing the cooling rate does not significantly change the crystal morphology, but it does cause a noticeable shift in the dominant crystal plane from (111) to (100).[19] However, for $Pb(Zn_{1/3}Nb_{2/3})O_3$, altering the cooling rate can significantly influence the hardness of the generated single crystal and also change its color.[20]

4. Magnetic properties

We systematically studied the magnetic properties of high-quality single crystals of $Ba_4CuNb_3O_{12}$ synthesized using method III, as shown in Fig. 7. When the magnetic field is along the *ab*-plane, the zero-field-cooling (ZFC) and field-cooling (FC) magnetic susceptibility (χ) gradually increase with decreasing temperature, and there is no magnetic phase transition. In addition, the magnetic susceptibility curves for FC and ZFC almost overlap. When the magnetic field is perpendicular to the *ab*-plane, the magnetic susceptibility behavior is identical to that when the field is applied along the *ab*-plane (Fig. 7(b)), which is quite unusual in single crystal systems, as strong anisotropy is typically observed in such materials. In a single crystal system, the crystal structure exhibits anisotropy, and the magnetic ions located at the lattice points often also exhibit magnetic anisotropy. For example, in the triangular lattice systems such as $Ba_3CoSb_2O_9$ (ref. 21 and 22) and Cs_2CuCl_4,[23] magnetic susceptibility anisotropy is observed even within the

paramagnetic temperature range. Furthermore, for the spin liquid candidate material $YMgGaO_4$,[24] the θ_{CW} values are approximately −1.47 K and −2.7 K when the magnetic field is applied parallel and perpendicular to the *c*-axis, respectively. The magnetism in $Ba_4CuNb_3O_{12}$ originates from Cu^{2+}, and the isotropic magnetism should be attributed to the randomness in atomic occupancy between Cu and Nb in the face-sharing CuO_6 and NbO_6 octahedra.

The temperature-dependent $1/\chi$ results indicate that the modified CW law, $\chi = \chi_0 + C/(T - \theta_{CW})$, is valid in the temperature range of 2 K to 300 K. Here, C is the Curie constant, and χ_0 represents the temperature-independent contributions from the core-diamagnetic (originating from both the sample and the sample holder) and Van Vleck susceptibility (Fig. 7(c)).[25,26] The effective magnetic moment (μ_{eff}) of Cu^{2+} is fitted to be 1.14 μ_B, with a θ_{CW} of −1.14 K and a χ_0 value of −0.00012 emu mol^{-1} Oe^{-1}. The negative θ_{CW} indicates the existence of antiferromagnetic correlation in the system. Importantly, in the ground state of $Ba_4CuNb_3O_{12}$, magnetic Cu^{2+} ions can undergo superexchange interactions with the nearest Cu^{2+} ions *via* the Cu^{2+}–O–O–(Nb^{5+}/Cu^+)–O–O–Cu^{2+} pathway, leading to the formation of antiferromagnetic correlations (Fig. S3†).[27] Certainly, this represents only the most probable superexchange pathway, and due to the randomness of the Cu^{2+} position, other possible superexchange pathways are not discussed in detail.

Notably, the obtained μ_{eff} = 1.14 μ_B is lower than the theoretical value of $g[S(S + 1)]^{1/2}$ = 1.73 μ_B, (assuming g = 2.0 and S = 1/2), where the spin–orbit coupling effect is ignored. In some spin-frustrated systems, the observed magnetic moment is lower than the theoretical value.[28,29] In an antiferromagnetic system, the frustration parameter is given by $f = |\theta_{CW}|/T_N$. For the $Ba_4CuNb_3O_{12}$ single crystal, since the T_N value cannot be determined from magnetic susceptibility data, estimating the frustration parameter is challenging. This also requires testing of the magnetic properties at lower temperatures, such as ^{3}He refrigeration or dilution refrigeration (^{3}He–^{4}He) equipment. Furthermore, it is important to note that if Cu atoms form a perfect triangular lattice, as seen in systems like $Ba_3CuSb_2O_9$,[29] spin frustration is highly likely to occur. In $Ba_4CuNb_3O_{12}$, Cu and Nb atoms jointly form a triangular lattice, the random

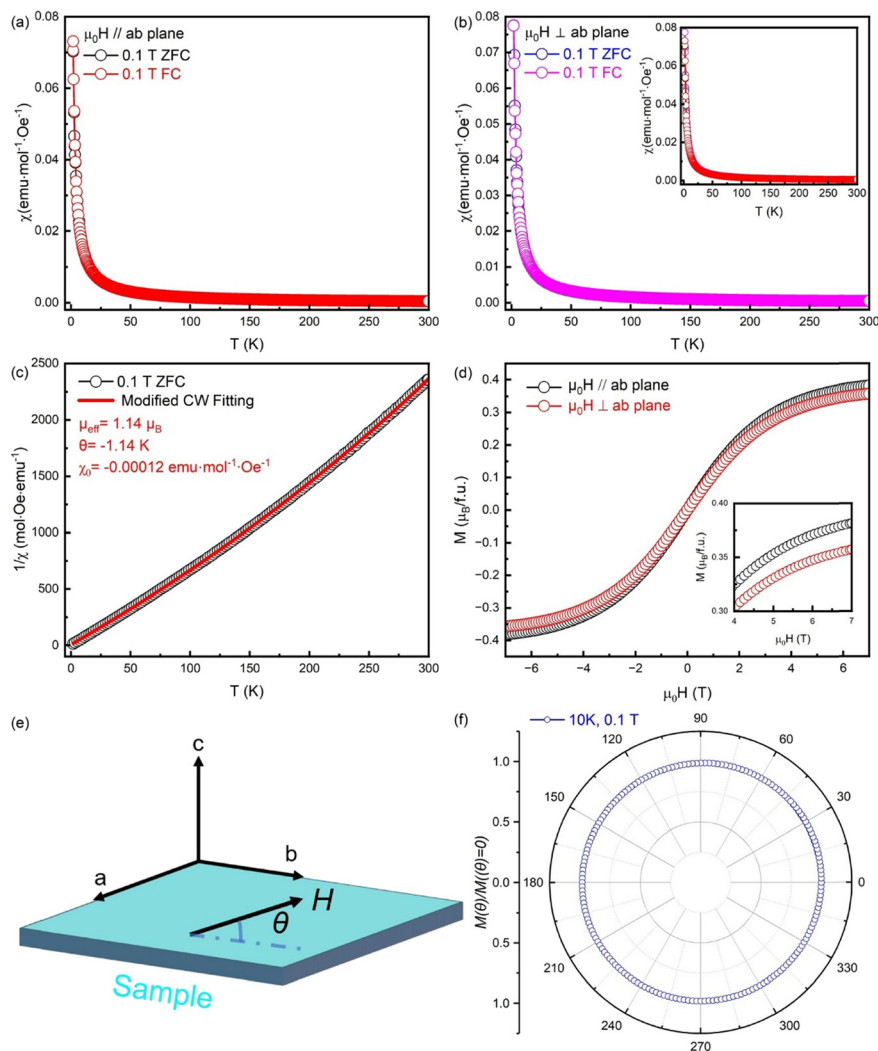**Fig. 7** ZFC and FC magnetic susceptibility of the $Ba_4CuNb_3O_{12}$ single crystal for a field (a) along the *ab*-plane and (b) perpendicular to the *ab*-plane. Inset of (b): the four magnetic susceptibility curves in the main figures (a) and (b), reflecting a high degree of overlap. (c) Temperature dependence of the inverse magnetic susceptibility for a field along the *ab*-plane. The red line represents the modified Curie–Weiss fitting. (d) Magnetization curves for a field applied along the *ab*-plane and perpendicular to the *ab*-plane. Inset: Magnification of the magnetic moment under a high magnetic field. (e) Schematic diagram of the measurement geometry for the (f) angular (θ)-dependent magnetization curve.

occupancy of Cu ions makes geometric frustration unlikely (Fig. 1(b)). However, the spin frustration may still arise due to competition between the nearest-neighbor and next-nearest-neighbor magnetic exchange interactions.[30–32]

To investigate the possible existence of a spin glass or cluster glass state in the $Ba_4CuNb_3O_{12}$ single crystal, we conducted AC magnetic susceptibility tests (Fig. S4†). The results show that when the AC magnetic field is applied along the *ab*-plane with no DC magnetic field, the Ba_4CuNb_3-O_{12} single crystal exhibits a peak at approximately 25 K with noticeable frequency dependence. However, since the peak position remains unchanged with frequency, the presence of a spin glass or cluster glass state can be ruled out. In fact, a similar frequency-dependent variation in the peak intensity has also been observed in $La_{1.5}Ca_{0.5}(Co_{0.5}Fe_{0.5})IrO_6$ (ref. 33) and $Sr_6(Co_{0.8}Fe_{0.2})_5O_{15}$,[26] though the peak position remains unchanged, and the underlying physical origin of this

behavior requires further investigation. Additionally, as for whether there is a short-range magnetic correlation, it is still difficult to give a clear conclusion based on the AC magnetic susceptibility.

The magnetization curves $M(H)$ measured at 2 K in the field range of −7 to 7 T show similar behavior for both field orientations (Fig. 7(d)). At 7 T, the magnetic moments along the *c*-axis and the *ab*-plane are 0.38 μ_B and 0.35 μ_B, respectively, as shown in the inset of Fig. 7(d). However, the slight difference in magnetic moments between the two, within $[(0.38 − 0.35)/0.38] \times 100\% = 7.89\%$, may be attributed to the fact that the spins of Cu ions tend to align in the *ab*-plane, indicating easy-plane anisotropy rather than easy-axis anisotropy.[34] Furthermore, we obtained the angle-dependence of the magnetization curve for a magnetic field 0.1 T along the *ab*-plane at 10 K, as shown in Fig. 7(e) and (f). When the magnetic field rotates within the *ab*-plane, the
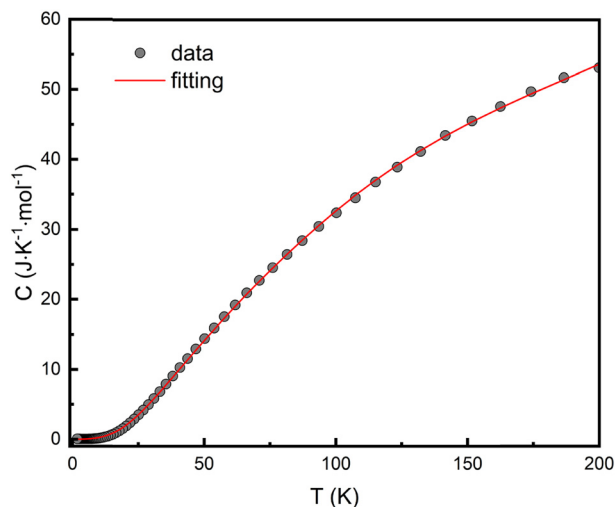
Fig. 8 Specific heat of the Ba$_4$CuNb$_3$O$_{12}$ single crystal. The red solid line represents the phonon specific heat contribution fitted using the Debye–Einstein model.

magnetic moment remains constant, indicating the isotropic nature of the in-plane magnetism.

5. Specific heat

The specific heat results of the Ba$_4$CuNb$_3$O$_{12}$ single crystal show no magnetic phase transition within the temperature range of 2 K to 200 K (Fig. 8), which is consistent with the magnetic behavior observed in the magnetic susceptibility curve. Importantly, our experimental data are well fitted by the Debye–Einstein model (red solid line in Fig. 8)

$$C_{\text{phonon}} = C_{\text{Debye}} + C_{\text{Einstein}}$$
$$= 3N_D R \left(\frac{T}{\Theta_D}\right)^3 \int_0^{\Theta_D/T} \frac{x^4 e^x}{(e^x - 1)^2} \, dx$$
$$+ \sum_{i=1}^{3} N_{Ei} R \left(\frac{\Theta_{Ei}}{T}\right)^2 \frac{e^{\frac{\Theta_{Ei}}{T}}}{\left(e^{\frac{\Theta_{Ei}}{T}} - 1\right)^2},$$

which describes the phonon behavior ($x = \hbar\omega/k_B T$). Here, ω, R, Θ_D, Θ_{Ei}, N_D and N_{Ei} represent the phonon frequency, universal gas constant, Debye temperature, Einstein temperature, the number of acoustic phonon branches, and the number of optical branches with the same Θ_{Ei}, respectively.[35,36] The best fitting parameters can be obtained as $\Theta_D = 199$ K, $\Theta_{E1} = 307$ K, $\Theta_{E2} = 510$ K, $\Theta_{E3} = 2100$ K, $N_D = 3$, $N_{E1} = 2$, $N_{E2} = 3$, and $N_{E3} = 52$. Furthermore, according to the formula $\Theta_D = \frac{\hbar v_p}{k_B} \left(\frac{6\pi^2 Ns}{V}\right)^{\frac{1}{3}}$, where N is the number of molecules per mole, s is the number of atoms in each molecule, and V is the volume of the crystal, and the average velocity v_p of phonons is calculated to be 2014.98 m s^{-1}.

In addition, since the ratio of Nb2 to Cu atoms in the triangular lattice formed by Nb2/Cu is about 1 : 2, this configuration effectively places two non-magnetic Nb2 atoms and one magnetic Cu atom at the triangular lattice sites. The

spin exchange interaction is between Cu atoms *via* O atoms. The insufficient number of Cu atoms occupying the lattice sites increases the exchange path, which weakens the correlation between the Cu atoms (Fig. S3†). In geometrically frustrated systems, such as those with triangular, kagome, and honeycomb lattices, the introduction of non-magnetic atoms can often have a significant impact on the spin exchange interactions between magnetic atoms, thereby altering the ground state of the system.[37,38]

Summary

In summary, we thoroughly explored the flux method for growing Ba$_4$CuNb$_3$O$_{12}$ single crystals and identified the most effective synthesis approach. Additionally, we investigated the magnetic properties of the Ba$_4$CuNb$_3$O$_{12}$ single crystal, both parallel and perpendicular to the *ab*-plane, with the findings confirming that the material exhibits an antiferromagnetic ground state. The reduced occupancy of Cu atoms at the triangular lattice sites extends the exchange path, weakening the interactions between the Cu atoms in Ba$_4$CuNb$_3$O$_{12}$. Furthermore, the specific heat data of Ba$_4$CuNb$_3$O$_{12}$ exhibit a strong correspondence with the Debye–Einstein phonon model, yielding estimates for the Debye temperature and the average phonon velocity as 199 K and 2014.98 m s^{-1}, respectively.

Data availability

The data that support the findings of this study are available from the corresponding author upon reasonable request.

Author contributions

Yuhu Huang and Wen Xie: data curation, investigation, software, and validation. Fei Zheng: investigation, formal analysis, software, and reviewing. Chao Zhang: data curation, formal analysis, and supervision. Han-Shu Xu: methodology, writing – original draft, supervision, and review and editing, funding acquisition, formal analysis, and visualization.

Conflicts of interest

There are no conflicts to declare.

References

1 L. T. Nguyen and R. J. Cava, Hexagonal perovskites as quantum materials, *Chem. Rev.*, 2020, **121**(5), 2935–2965.

2 K. Matsuzaki, K. Saito, Y. Ikeda, Y. Nambu and M. Yashima, High proton conduction in the octahedral layers of fully hydrated hexagonal perovskite-related oxides, *J. Am. Chem. Soc.*, 2024, **146**(27), 18544–18555.

3 H.-C. zur Loye, Q. Zhao, D. E. Bugaris and W. M. Chance, 2 H-perovskite related oxides: Synthesis, structures, and predictions, *CrystEngComm*, 2012, **14**(1), 23–39.

4 H.-S. Xu, Y. Huang, J. Li and F. Zheng, Magnetic Properties and Specific Heat of Quasi-Two-Dimensional Triangular Lattice Antiferromagnet $Ba_3CoNb_2O_9$ Single Crystals, *J. Phys. Chem. C*, 2025, **129**(2), 1562–1567.

5 Y. Huang and H.-S. Xu, Growth of Fe-Substituted $Sr_6Co_5O_{15}$ Hexagonal Perovskite Single Crystals by a Flux Method, *Cryst. Growth Des.*, 2023, **23**(5), 3747–3753.

6 J. Li, H.-S. Xu, J. Hu, Y. Huang, W. Xie, D. Yu and K. Tang, Comparative Study on the Electrocatalytic Performance of ABO_3-Based Hexagonal Perovskite Oxides with Different $[AO_3]$ Layers, *Inorg. Chem.*, 2024, **63**(50), 23601–23613.

7 W. Cao, X. Yang, F. Lu, W. Zhu, L. Liu, X. Kuang and M. Allix, 8H–10H stacking periodicity control in twinned hexagonal perovskite dielectrics, *Inorg. Chem.*, 2018, **57**(7), 4117–4124.

8 E. F. Jendrek Jr., A. D. Potoff and L. Katz, A single-crystal study of eight-layer barium niobium lithium oxide, Ba_4Nb_3-LiO_{12}, *J. Solid State Chem.*, 1974, **9**(4), 375–379.

9 T. Negas, R. Roth, H. Parker and W. Brower, Crystal chemistry of lithium in octahedrally coordinated structures. I. Synthesis of Ba8 (Me_6Li_2) O_{24} (Me = Nb or Ta) and Ba_{10} (W_6Li_4) O_{30}. II. The tetragonal bronze phase in the system BaO Nb_2O_5 Li_2O, *J. Solid State Chem.*, 1973, **8**(1), 1–13.

10 N. Teneze, P. Boullay, V. Petricek, G. Trolliard and D. Mercurio, Structural study of the cation ordering in the ternary oxide $Ba_8Ti_3Nb_4O_{24}$, *Solid State Sci.*, 2002, **4**(9), 1129–1136.

11 R. Rawal, A. Feteira, A. A. Flores, N. C. Hyatt, A. R. West, D. C. Sinclair, K. Sarma and N. M. Alford, Dielectric properties of the "twinned" 8H-hexagonal perovskite Ba_8Nb_4-Ti_3O_{24}, *J. Am. Ceram. Soc.*, 2006, **89**(1), 336–339.

12 P. Battle, S. Kim and A. Powell, The crystal structure and electronic properties of $Ba_4Ru_3MO_{12}$ (M = Li, Na, Mg, Zn), *J. Solid State Chem.*, 1992, **101**(1), 161–172.

13 F. Tao, C. Liang, X. Wang, X. Li, F. Porcher, M. Allix, F. Lu, H. Gong, L. Liu and X. Kuang, 8-layer shifted hexagonal perovskite $Ba_8MnNb_6O_{24}$: long-range ordering of high-spin d5 Mn^{2+} layers and electronic structure, *Inorg. Chem.*, 2018, **57**(10), 5732–5742.

14 R. Rawl, L. Ge, Z. Lu, Z. Evenson, C. Dela Cruz, Q. Huang, M. Lee, E. Choi, M. Mourigal and H. Zhou, $Ba_8MnNb_6O_{24}$: A model two-dimensional spin-5 2 triangular lattice antiferromagnet, *Phys. Rev. Mater.*, 2019, **3**(5), 054412.

15 N. Kumada, W. Zhang, Q. Dong, T. Mochizuki, Y. Yonesaki, T. Takei and N. Kinomura, Crystal structure and X-ray diffraction data of a new hexagonal perovskite compound, $Ba_4CuNb_3O_{12}$, *Powder Diffr.*, 2011, **26**(3), 244–247.

16 L. Balents, Spin liquids in frustrated magnets, *Nature*, 2010, **464**(7286), 199–208.

17 Z. Zhu, P. A. Maksimov, S. R. White and A. L. Chernyshev, Disorder-Induced Mimicry of a Spin Liquid in $YbMgGaO_4$, *Phys. Rev. Lett.*, 2017, **119**(15), 157201.

18 Y. Li, D. Adroja, R. I. Bewley, D. Voneshen, A. A. Tsirlin, P. Gegenwart and Q. Zhang, Crystalline Electric-Field Randomness in the Triangular Lattice Spin-Liquid $YbMgGaO_4$, *Phys. Rev. Lett.*, 2017, **118**(10), 107202.

19 B. Sun, R. Boutellier, P. Sciau, E. Burkhardt, V. Rodriguez and H. Schmid, High temperature solution growth of perovskite Pb_2CoWO_6 single crystals, *J. Cryst. Growth*, 1991, **112**(1), 71–83.

20 M. L. Mulvihill, S. E. Park, G. Risch, Z. Li, K. U. K. Uchino and T. R. S. T. R. Shrout, The role of processing variables in the flux growth of lead zinc niobate-lead titanate relaxor ferroelectric single crystals, *Jpn. J. Appl. Phys.*, 1996, **35**(7R), 3984.

21 A. Sera, Y. Kousaka, J. Akimitsu, M. Sera, T. Kawamata, Y. Koike and K. Inoue, S = 1 2 triangular-lattice antiferromagnets Ba_3-$CoSb_2O_9$ and $CsCuCl_3$: Role of spin-orbit coupling, crystalline electric field effect, and Dzyaloshinskii-Moriya interaction, *Phys. Rev. B*, 2016, **94**(21), 214408.

22 H. D. Zhou, C. Xu, A. M. Hallas, H. J. Silverstein, C. R. Wiebe, I. Umegaki, J. Q. Yan, T. P. Murphy, J.-H. Park and Y. Qiu, Successive Phase Transitions and Extended Spin-Excitation Continuum in the $S = \frac{1}{2}$ Triangular-Lattice Antiferromagnet $Ba_3CoSb_2O_9$, *Phys. Rev. Lett.*, 2012, **109**(26), 267206.

23 Y. Tokiwa, T. Radu, R. Coldea, H. Wilhelm, Z. Tylczynski and F. Steglich, Magnetic phase transitions in the two-dimensional frustrated quantum antiferromagnet Cs_2CuCl_4, *Phys. Rev. B: Condens. Matter Mater. Phys.*, 2006, **73**(13), 134414.

24 Y. Li, G. Chen, W. Tong, L. Pi, J. Liu, Z. Yang, X. Wang and Q. Zhang, Rare-earth triangular lattice spin liquid: a single-crystal study of $YbMgGaO_4$, *Phys. Rev. Lett.*, 2015, **115**(16), 167203.

25 S. Mugiraneza and A. M. Hallas, Tutorial: a beginner's guide to interpreting magnetic susceptibility data with the Curie-Weiss law, *Commun. Phys.*, 2022, **5**(1), 95.

26 H.-S. Xu, S. Zeng, S. Fang, Y. Huang, W. Xie, H. Huang, Y. Lu and K.-B. Tang, Tunability of magnetization in hexagonal perovskite $Sr_6Co_5O_{15}$ ceramics through 20% Fe-substitution, *J. Magn. Magn. Mater.*, 2023, **573**, 170648.

27 J. Cheng, W. Tian, J. Zhou, V. M. Lynch, H. Steinfink, A. Manthiram, A. F. May, V. O. Garlea, J. C. Neuefeind and J. Yan, Crystal and magnetic structures and physical properties of a new pyroxene $NaMnGe_2O_6$ synthesized under high pressure, *J. Am. Chem. Soc.*, 2013, **135**(7), 2776–2786.

28 H. D. Zhou, B. W. Vogt, J. A. Janik, Y. J. Jo, L. Balicas, Y. Qiu, J. R. D. Copley, J. S. Gardner and C. R. Wiebe, Partial Field-Induced Magnetic Order in the Spin-Liquid Kagome Nd_3Ga_5-SiO_{14}, *Phys. Rev. Lett.*, 2007, **99**(23), 236401.

29 J. E. Greedan, Geometrically frustrated magnetic materials, *J. Mater. Chem.*, 2001, **11**(1), 37–53.

30 Y. Ishiguro, K. Kimura, S. Nakatsuji, S. Tsutsui, A. Q. Baron, T. Kimura and Y. Wakabayashi, Dynamical spin–orbital correlation in the frustrated magnet $Ba_3CuSb_2O_9$, *Nat. Commun.*, 2013, **4**(1), 2022.

31 Y. Shimizu, K. Miyagawa, K. Kanoda, M. Maesato and G. Saito, Spin liquid state in an organic Mott insulator with a triangular lattice, *Phys. Rev. Lett.*, 2003, **91**(10), 107001.

32 R. Coldea, D. Tennant, A. Tsvelik and Z. Tylczynski, Experimental realization of a 2D fractional quantum spin liquid, *Phys. Rev. Lett.*, 2001, **86**(7), 1335.

33 L. Bufaiçal, M. Heringer, J. Jesus, A. Caytuero, C. Macchiutti, E. Bittar and E. Baggio-Saitovitch, Structural, electronic and magnetic properties of $La_{1.5}Ca_{0.5}(Co_{0.5}Fe_{0.5})$ IrO_6 double perovskite, *J. Magn. Magn. Mater.*, 2022, **556**, 169408.

34 K. Y. Povarov, L. Facheris, S. Velja, D. Blosser, Z. Yan, S. Gvasaliya and A. Zheludev, *et al.*, *Phys. Rev. Res.*, 2020, **2**(4), 043384.

35 P. Svoboda, P. Javorský, M. Diviš, V. Sechovský, F. Honda, G. Oomi and A. A. Menovsky, Importance of anharmonic terms in the analysis of the specific heat of UNi_2Si_2, *Phys. Rev. B: Condens. Matter Mater. Phys.*, 2001, **63**(21), 212408.

36 F. W. de Wette and A. D. Kulkarni, Phonon dispersion, phonon specific heat, and Debye temperature of high-temperature superconductors, *Phys. Rev. B: Condens. Matter Mater. Phys.*, 1992, **46**(22), 14922–14925.

37 Z. Zhang, D. Louca, A. Visinoiu, S. H. Lee, J. D. Thompson, T. Proffen, A. Llobet, Y. Qiu, S. Park and Y. Ueda, Local order and frustration in the geometrically frustrated spinels $Cd_{1-x}Zn_xV_2O_4$, *Phys. Rev. B: Condens. Matter Mater. Phys.*, 2006, **74**(1), 014108.

38 J. P. Sheckelton, J. R. Neilson and T. M. McQueen, Electronic tunability of the frustrated triangular-lattice cluster magnet $LiZn_{2-x}Mo_3O_8$, *Mater. Horiz.*, 2015, **2**(1), 76–80.